

Privacy Preserving Domain Adaptation for Semantic Segmentation of Medical Images

Serban Stan
University of Southern California
sstan@usc.edu

Mohammad Rostami
USC Information Sciences Institute
rostamim@usc.edu

Abstract

Convolutional neural networks (CNNs) have led to significant improvements in tasks involving semantic segmentation of images. CNNs are vulnerable in the area of biomedical image segmentation because of distributional gap between two source and target domains with different data modalities which leads to domain shift. Domain shift makes data annotations in new modalities necessary because models must be retrained from scratch. Unsupervised domain adaptation (UDA) is proposed to adapt a model to new modalities using solely unlabeled target domain data. Common UDA algorithms require access to data points in the source domain which may not be feasible in medical imaging due to privacy concerns. In this work, we develop an algorithm for UDA in a privacy-constrained setting, where the source domain data is inaccessible. Our idea is based on encoding the information from the source samples into a prototypical distribution that is used as an intermediate distribution for aligning the target domain distribution with the source domain distribution. We demonstrate the effectiveness of our algorithm by comparing it to state-of-the-art medical image semantic segmentation approaches on two medical image semantic segmentation datasets.

1. Introduction

Employing CNNs in semantic segmentation tasks has been proven to be extremely helpful in various applications, including object tracking [69, 2, 76], self-driving cars [31, 22], and medical image analysis [30, 59, 1, 29]. This success, however, is conditioned on the availability of huge manually annotated datasets to supervise the training of state-of-the-art (SOTA) networks structures [51, 64]. This condition is not always realized in practice, especially in fields such as medical image segmentation, where annotating data requires the input of trained experts and privacy regulations make sharing data for crowd-sourcing extremely restricted, and at times impossible. A characteristic

of data in the area of medical image segmentation is the existence of *domain shift* between different imaging modalities which results from using imaging devices that are based on totally different electromagnetic principles, e.g., CT vs MRI. When domain gap exists between the distributions of the training (source) and the testing (target) data, the performance of CNNs can degrade significantly. This makes continual data annotation necessary for mode retraining.

Domain shift is a major area of concern, as data annotation is a challenging procedure even for the simplest semantic segmentation tasks [38]. Annotating medical images is also expensive, as annotation can be performed only by physicians, who undergo years of training to obtain domain expertise. Unsupervised domain adaptation (UDA) is a learning setting aimed at reducing *domain gap* without data annotation in the target domain. The goal is to adapt a source-trained model for improved generalization in the target domain using solely unannotated data [20, 68, 56, 71]. The core idea in UDA is to achieve knowledge transfer from the source domain to the target domain by aligning the latent features of the two domains in an embedding space. This idea has been implemented either using adversarial learning [23, 13, 67, 4], directly minimizing the distance of distributions of the latent features with respect to a probability metric [8, 62, 36], or a combination of the two [11, 58].

While existing UDA algorithms have been successful in reducing domain gap, the vast majority of these algorithms require sharing data between the source and target domains to enforce distribution alignment. This requirement limits the applicability of most existing works when sharing data may not be possible, e.g., sharing data is heavily regulated in healthcare domains due to privacy or security concerns. Until recently, there has been little exploration of UDA when access to the source domain is limited [33, 57, 49]. These works benefit from generative adversarial learning to remember the source domain. However, both address UDA for only classification tasks which limits their applicability to the problem of organ semantic segmentation [74].

Contribution: we develop a UDA algorithm for semantic segmentation when privacy and security are major

concerns making sharing data infeasible. Additionally, our work provides a method for semantic segmentation in a continual learning regime [54, 55]. Our approach is able to mitigate domain gap without having direct access to the source data. We learn a prototypical distribution for the source domain, and transfer knowledge between the source and target domains by distribution alignment between the learned prototypical distribution and the latent features of the target domain. We validate our algorithm on two medical image segmentation datasets, and observe comparable performance to SOTA methods based on joint training.

2. Related Work

SOTA semantic segmentation algorithms use deep neural network architectures to exploit large annotated datasets [40, 45, 37, 19]. These approaches are based on training a CNN encoder using manually annotated segmentation maps to learn a latent embedding of the data. An up-sampling decoder combined with a classifier is then used to infer pixel-wise estimations for the true semantic labels. Performance of such methods is high when large amounts of annotated data are available for supervised training. However, these methods are not suitable when the goal is to transfer knowledge between different domains [56, 46]. Model adaptation to target domains has been explored in both semi-supervised and unsupervised settings. Semi-supervised approaches rely on the presence of a small number of annotated target data samples [44, 70]. For example, a weakly supervised signal on the target domain can be obtained using bounding boxes. However, manual data annotation of a small number of images is still a considerable bottleneck in the area of medical imaging because only trained professionals can perform this task. For this reason, UDA algorithms are more appealing for healthcare applications.

UDA approaches have explored two main strategies to reduce the domain gap. A large number of works rely on generative adversarial networks (GANs) [72, 27]. The core idea is to train a GAN such that data points of both domains can be mapped into a domain-agnostic embedding space [23]. To this end, a cross-domain discriminator network is trained to classify whether an input data point belongs to the source domain or the target domain. The discriminator network receives its input from a feature generator network. The discriminator network is fooled by the feature generator network which is trained as an adversary to generate domain-agnostic features at its output. As a result, a classifier network that is trained using the source domain annotated data at the output of the generator network would generalize well in the target domain [41, 14]. An area of weakness for GANs is mode collapse which happens and need for fine-tuning the model hyper-parameters.

A second approach for UDA is to align the distributions of the two domains directly in a latent embedding

space [48]. A shared encoder is used to generate latent embeddings for both domains and then it is trained such that the distance between the domain-specific distributions is minimized with respect to a suitable probability distance metrics at the output of the shared encoder [36, 17, 53, 52, 35, 39]. Selecting the proper distance metrics has been the major focus of research for these approaches. Optimal transport has been found particularly suitable for UDA based on deep learning due to its suitability for gradient-based optimization [12]. Building our prior work, we benefit from the Sliced Wasserstein distance (SWD) [61, 50] variant of the optimal transport [36]. SWD has properties similar to optimal transport, but also has a closed form solution that can be used to compute it efficiently.

Both of the above mentioned approaches have been found helpful in various medical semantic segmentation applications [24, 73, 5, 26]. However, both UDA strategies require direct access to the source domain data to compute their corresponding loss functions. To relax this requirement, UDA has been recently explored in a source-free setting in order to address applications in which the source domain is not directly accessible [33, 57]. Both Kundu et al. [33] and Saltori et al. [57] target image classification, and benefit from generative adversarial learning to generate pseudo-data points that are similar to the source domain data in the absence of actual source samples. While both approaches are suitable for classification problems, extending them to semantic segmentation of medical images is not trivial. First, training models that can generate realistic medical images is considerably more challenging due to importance of fine details. Second, one may argue that if the generated images are too similar to the real images, the privacy of human subjects in the training data may still be compromised. Our work is based on using a dramatically different approach. We develop a source-free UDA algorithm that performs the distribution alignment of two domains in an embedding space by using an intermediate prototypical distribution to relax the need for source data.

3. Problem Formulation

Consider a source domain $D^S = (X^S, Y)$ with annotated data and a target domain with unannotated data $D^T = (X^T, Y)$ that despite having different input spaces X^S and X^T , e.g., due to using different medical imaging techniques, share the same segmentation map space Y , e.g., the same tissue/organ classes. Following the standard UDA pipeline, the goal is to learn a segmentation mapping function for the target domain by transferring knowledge from the source domain. To this end, we must learn a function $f_{\theta}(\cdot) : \{X^S \cup X^T\} \rightarrow \{Y\}$ with learnable parameters θ , e.g., a deep neural network, such that given an input image x^* , the function returns a segmentation mask \hat{y} that best ap-

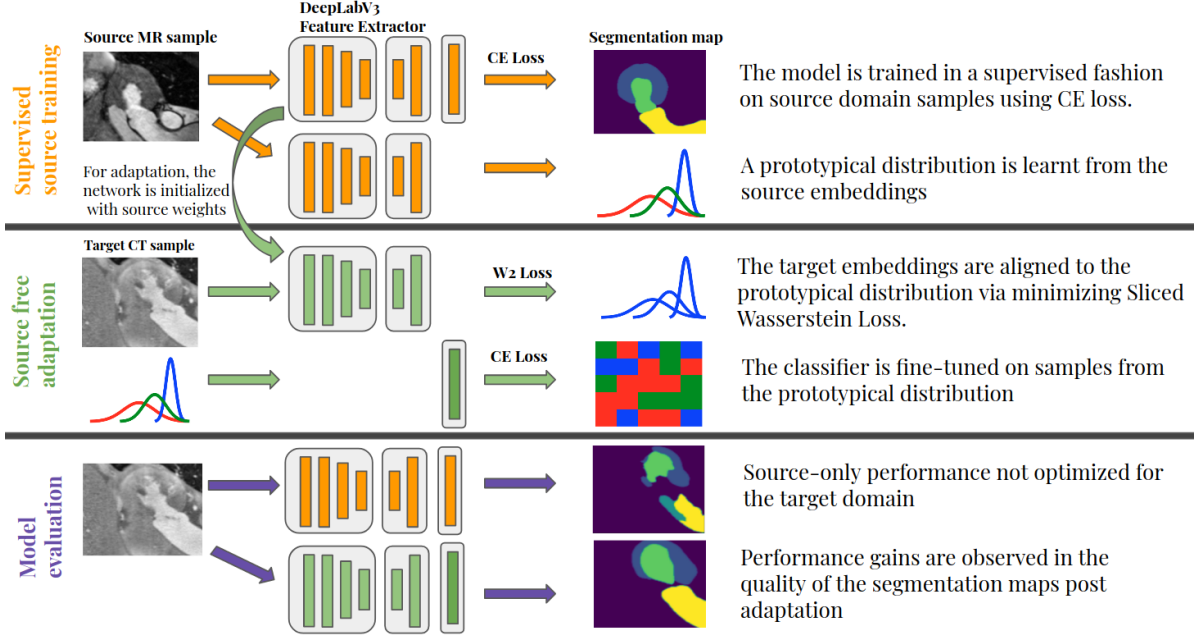


Figure 1: Diagram of our proposed method. We first perform supervised training on source MR images. Using the source embeddings we characterize a prototypical distribution via a GMM distribution in the latent space. We then perform source free adaptation by matching the embedding of the target CT images to the learnt GMM distribution, and fine tuning of the classifier on GMM samples. Finally, we verify the improved performance that our model gains from model adaptation.

proximates the ground truth segmentation mask y^* . Given the annotated training dataset $\{(x^s, y^s)\}_{i=1}^N$ in the source domain, it is straightforward to train a segmentation model that generalizes well in the source domain through solving an empirical risk minimization (ERM) problem:

$$\hat{\theta} = \arg \min_{\theta} \frac{1}{N} \sum_{i=1}^N \mathcal{L}(y^s, f_{\theta}(x^s)), \quad (1)$$

where \mathcal{L} is a proper loss function. For example, we can use the pixel-wise cross-entropy loss, defined as:

$$\mathcal{L}_{ce}(y^*, \hat{y}) = - \sum_{i=1}^W \sum_{j=1}^H \sum_{k=1}^K y_{ijk}^* \log \hat{y}_{ijk},$$

where, K denotes the number of segmentation classes, and W, H represent the width and the height the input images, respectively. Each pixel label y_{ij}^* will be represented as a one hot vector of size K and \hat{y}_{ij} is the prediction vector which assigns a probability weight to each label. Due to the existence of domain gap across the two domains, i.e. discrepancy between the source domain distribution $p^s(X)$ and the target domain distribution $p^t(X)$, the source-trained model in Eq. (1) may generalize poorly in the target domain. We want to benefit from the information encoded in the target domain unannotated dataset $\{x^t\}_{i=1}^M$ to improve the model generalization in the target domain.

We follow the common strategy of domain alignment in a shared embedding space to tackle UDA. Consider our model f to be a deep convolutional neural network (CNN). Let $f = \phi \circ \chi \circ \psi$, where $\psi(\cdot) : \mathbb{R}^{W \times H \times C} \rightarrow \mathbb{R}^{U \times V}$ is a CNN encoder, $\chi(\cdot) : \mathbb{R}^{U \times V} \rightarrow \mathbb{R}^{W \times H}$ is an up-scaling CNN decoder, and $\phi(\cdot) : \mathbb{R}^{W \times H} \rightarrow \mathbb{R}^{W \times H}$ is a classification network that takes as inputs latent space representations and assigns label-probability values. We model the shared embedding space as the output space of the sub-network $\chi \circ \psi(\cdot)$. Solving UDA then would reduce to aligning the distributions of the source domain and target domain in the embedding space because. This translates into minimizing the distributional discrepancy between the distributions $\chi \circ \psi(p^s(\cdot))$ and $\chi \circ \psi(p^t(\cdot))$ in the embedding space.

A large group of UDA algorithms select a probability distribution metric $D(\cdot, \cdot)$, e.g. SWD or KL-divergence, and then use the source and the target domain data points, $X^S = [x_1^s, \dots, x_N^s]$ and $X^T = [x_1^t, \dots, x_N^t]$, to minimize the loss term $D(\chi \circ \psi(p^s(\cdot)), \chi \circ \psi(p^t(\cdot)))$ as a regularizer. However, this will have constrained the user to have access to the source domain data for computing $D(\chi \circ \psi(p^s(\cdot)), \chi \circ \psi(p^t(\cdot)))$ that couples the two domains. In medical image segmentation and other similar avenues in which privacy or security are crucial, sharing the source domain data is not possible. As a result, UDA based on the above pipeline for the domain alignment of feature embed-

dings would be inoperative. To tackle this challenge, we provide a solution to align the two domains without sharing the source domain data, that benefits from an intermediate distribution that is learned in the source domain.

4. Proposed Algorithm

Our proposed approach is based on using the prototypical distribution $\mathcal{P}_{\mathcal{Z}}$ as a surrogate for the learned distribution of the source domain in the embedding space. Upon training f_{θ} using Eq. (1), the embedding space would become discriminative for the source domain. This means that the source distribution in the embedding will be a multimodal distribution, where each mode denotes one of the classes. This distribution can be modeled as a Gaussian mixture model (GMM). To develop a source-free UDA algorithm, we can draw random samples from the GMM and instead of relying on the source data, align the target domain distribution with the prototypical distribution in the embedding space. In other words, we estimate the term $D(\chi \circ \psi(p^s(\cdot)), \chi \circ \psi(p^t(\cdot)))$ with $D(\mathcal{P}_{\mathcal{Z}}(\cdot), \chi \circ \psi(p^t(\cdot)))$ which does not depend on source samples. In our formulation, we use the Sliced Wasserstein Distance as the distribution metric for minimizing the domain discrepancy. A visual description for our approach is presented in Figure 1.

More specifically, the feature extractor $\psi \circ \chi$ will transform the input distribution $p^s(\cdot)$ to the prototypical distribution $\mathcal{P}_{\mathcal{Z}}(\cdot) = \chi \circ \psi(p^s(\cdot))$ based on which the classifier ϕ assigns the label probabilities. This distribution will have K modes. Our key idea is to approximate $\mathcal{P}_{\mathcal{Z}}(\cdot)$ via a GMM with K components, each component encoding a class:

$$\mathcal{P}_{\mathcal{Z}}(z) = \sum_{k=1}^K \alpha_k p_k(z) = \sum_{k=1}^K \alpha_k \mathcal{N}(z | \mu_k, \Sigma_k),$$

where α_k represents the mixture probabilities for each class $k \in \{1, 2, \dots, K\}$, μ_k represents the mean of the Gaussian k , and Σ_k is the covariance matrix of the k^{th} component. When the network f is trained on the source domain, we can estimate the GMM parameters from the latent features obtained from the source training samples $\{\phi(\chi(x^s))_{ijt}, y_{ij}^s\}$. Moreover, we do not need to estimate the GMM parameters using unsupervised algorithms such as expectation maximization (EM), as we have direct access to the labels Y^S .

To improve class separations in the prototypical distribution $\mathcal{P}_{\mathcal{Z}}$, we only use high-confidence samples in each class for estimating parameters of $p_k(\cdot)$. We use a confidence threshold parameter ρ , and discard all samples for which the classifier confidence on its prediction p_{ij} is strictly less than ρ . This step helps cancel out class outliers. Let $\mathcal{S}_{\rho} = \{(x_{ij}^s, y_{ij}^s) | \psi(\chi(\phi(x_{ij}^s))) > \rho\}$ be the source data pixels on which the classifier ϕ assigns confidence greater than ρ . Also, let $\mathcal{S}_{\rho,k} = \{(x, y) | (x, y) \in \mathcal{S}_{\rho}, y = k\}$. We can then generate empirical estimates for μ_k and Σ_k as:

$$\hat{\alpha}_k = \frac{|\mathcal{S}_{\rho,k}|}{|\mathcal{S}_{\rho}|}, \hat{\mu}_k = \frac{1}{|\mathcal{S}_{\rho,k}|} \sum_{(x,y) \in \mathcal{S}_{\rho,k}} \chi(\phi(x))$$

$$\hat{\Sigma}_k = \frac{1}{|\mathcal{S}_{\rho,k}|} (\chi(\phi(x)) - \hat{\mu}_k)^T (\chi(\phi(x)) - \hat{\mu}_k)$$
(2)

Given the estimated parameters $\hat{\alpha}_k, \hat{\mu}_k, \hat{\Sigma}_k$ for the prototypical distribution, we can perform domain alignment. The goal is to adapt the model such that the target latent distribution $\chi(\psi(p^t(X)))$ matches the distribution $\mathcal{P}_{\mathcal{Z}}$ in the embedding space. To this end, we can generate a pseudo-dataset $D^P = (Z^P, Y^P)$ by drawing random samples from the GMM and align $\chi(\psi(X^T))$ with Z^P to reduce the domain gap. The alignment loss can then be formalized as:

$$\mathcal{L}_{adapt} = \mathcal{L}_{ce}(\psi(Z^P), Y^P) + \lambda \mathcal{D}(\chi(\psi(X^T)), Z^P)$$
(3)

The first term in Eq. 3 involves fine-tuning the classifier on samples of pseudo-dataset (Z^P, Y^P) to ensure that it would continue to generalize well. The second term enforces the distributional alignment. As a result, the updated model will generalize on the target domain. Since the source samples are not used in Eq. 3, privacy of the source domain will also be preserved. Note that the source and target domains share initial similarities, otherwise domain alignment as described above may produce overlap of disjoint classes.

The last ingredient for our approach is selection of the distance metric $\mathcal{D}(\cdot, \cdot)$. We used SWD for this purpose. SWD is an approximation to high dimensional Wasserstein Distance (WD) [43, 18] which has been shown to be helpful in deep learning. Computing WD directly is challenging, however WD can be empirically approximated via SWD [32]. SWD achieves this by approximating the high dimensional optimal transport problem via 1D Wasserstein Distance instances which are obtained by performing L random unit sphere projections o_i of its two input distributions as:

$$\mathcal{D}(P, Q) = \frac{1}{L} \sum_{i=1}^L \mathcal{D}_{1-WD}(\langle P, o_i \rangle, \langle Q, o_i \rangle),$$
(4)

where P and Q are data distributions and $\langle P, o_i \rangle$ and $\langle Q, o_i \rangle$ denote the one-dimensional distributional slices, respectively. In Eq. (4) the term \mathcal{D}_{1-WD} denotes the 1D WD metric. Since WD has a closed form solution in the dimension of one, Eq. (4) can be computed efficiently. We present the pseudocode of the above described approach, called Source Free semantic Segmentation (SFS), in Algorithm 1.

5. Theoretical Analysis

We propose that Algorithm 1 is effective because an upper-bound of the expected error for the target domain is minimized as a result of domain alignment.

Algorithm 1 SFS (λ, ρ)

- 1: **Initial Training:**
 - 2: **Input:** source domain dataset $\mathcal{D}^S = (\mathbf{X}^S, \mathbf{Y}^S)$,
 - 3: **Training on Source Domain:**
 - 4: $\hat{\theta}_0 = \arg \min_{\theta} \sum_i \mathcal{L}(f_{\theta}(\mathbf{x}_i^s), \mathbf{y}_i^s)$
 - 5: **Prototypical Distribution Estimation:**
 - 6: Use Eq. (2), set $\rho = .97$ and estimate $\hat{\alpha}_j, \hat{\mu}_j$, and $\hat{\Sigma}_j$
 - 7: **Model Adaptation:**
 - 8: **Input:** target dataset $\mathcal{D}^T = (\mathbf{X}^T)$
 - 9: **Pseudo-Dataset Generation:**
 - 10: $\mathcal{D}^P = (\mathbf{Z}^P, \mathbf{Y}^P) =$
 - 11: $((\mathbf{z}_1^p, \dots, \mathbf{z}_N^p), [\mathbf{y}_1^p, \dots, \mathbf{y}_N^p])$, where:
 - 12: $\mathbf{z}_i^p \sim \mathcal{P}_Z(\mathbf{z}), 1 \leq i \leq N_p$
 - 13: **for** $itr = 1, \dots, ITR$ **do**
 - 14: draw random batches from \mathcal{D}^T and \mathcal{D}^P
 - 15: Update the model by solving Eq. (3)
 - 16: **end for**
-

We analyze the problem in a standard PAC-learning setting. Consider that the set of classifier sub-networks $\mathcal{H} = \{\psi_{\mathbf{w}}(\cdot) | \psi_{\mathbf{w}}(\cdot) : \mathcal{Z} \rightarrow \mathbb{R}^k, \mathbf{w} \in \mathbb{R}^W\}$ to be our hypothesis space. Let e_S and e_T denote the expected error of the optimal model that belongs to this space on the source and target domains, respectively. Let $\psi_{\mathbf{w}^*}$ to be the model which minimizes the combined source and target expected error $e_C(\mathbf{w}^*)$, defined as: $\mathbf{w}^* = \arg \min_{\mathbf{w}} e_C(\mathbf{w}) = \arg \min_{\mathbf{w}} \{e_S + e_T\}$. This model is the best model within the hypothesis space in terms generalizability in both domains. Additionally, consider that $\hat{\mu}_S = \frac{1}{N} \sum_{n=1}^N \delta(\chi(\psi_{\mathbf{v}}(\mathbf{x}_n^s)))$ and $\hat{\mu}_T = \frac{1}{M} \sum_{m=1}^M \delta(\chi(\psi_{\mathbf{v}}(\mathbf{x}_m^t)))$ are the empirical source distribution and the empirical target distribution in the embedding space, both built from the available data points. Let $\hat{\mu}_P = \frac{1}{N_p} \sum_{q=1}^{N_p} \delta(\mathbf{z}_n^q)$ denote the empirical prototypical distribution, built from the generated pseudo-dataset. Since we build our pseudo-data set based on points with confident labels, we can set: $\rho = \mathbb{E}_{\mathbf{z} \sim \mathcal{P}_Z(\mathbf{z})} (\mathcal{L}(\psi_{\hat{\mathbf{w}}_0}(\mathbf{z})))$.

Theorem 1: Consider that we generate a pseudo-dataset using the prototypical distribution and perform UDA according to algorithm 1, then:

$$e_T \leq e_S + W(\hat{\mu}_S, \hat{\mu}_P) + W(\hat{\mu}_T, \hat{\mu}_P) + (1 - \rho) + e_{C'}(\mathbf{w}^*) + \sqrt{(2 \log(\frac{1}{\xi}) / \zeta) (\sqrt{\frac{1}{N}} + \sqrt{\frac{1}{M}} + 2\sqrt{\frac{1}{N_p}})}, \quad (5)$$

where $W(\cdot, \cdot)$ denotes the WD distance and ξ is a constant, dependent on the loss function $\mathcal{L}(\cdot)$.

Proof: proof is included in the Appendix.

According to Theorem 1, algorithm 1 minimizes the upper bound expressed in Eq. (5) for the target domain expected risk. The source expected risk is minimized when we train the model on the source domain. The second term

in Eq. (5) is minimized when the GMM is fitted on the source domain distribution. The third term in the Eq. (5) upperbound is minimized because it is the second term in Eq. (3). The fourth term is small if we let $\rho \approx 1$. The term $e_{C'}(\mathbf{w}^*)$ will be small if the domains are related to the extent that a joint-trained model can generalize well on both domains, e.g., there shouldn't be label mismatch between similar classes across the two domains. The last term in Eq. (5) is negligible if the training datasets are large enough.

6. Experimental Validation

Our code is available on [github](https://github.com/serbanstan/uda-medical-image-segmentation-sfs)¹.

6.1. Datasets

We evaluate our algorithm on the following datasets.

Multi-Modality Whole Heart Segmentation Dataset (MMWHS) [78]: this dataset consists of multi-modality whole heart images obtained on different imaging devices at different imaging sites. Segmentation maps are provided for 20 MRI 3D heart images and 20 CT 3D heart images which have domain gap. Following the UDA setup, we use the MRI images as the source domain and CT images as the target domain. We perform UDA with respect to four of the available segmentation classes: ascending aorta (AA), left ventricle blood cavity (LVC), left atrium blood cavity (LAC), myocardium of the left ventricle (MYO).

We will use the same experimental setup and parsed dataset used by Dou et al. [15] for fair comparison. For the MRI source domain we use augmented samples from 16 MRI 3D instances. The target domain consists of augmented samples from 14 3D CT images, and we report results on 4 CT instances, as proposed in by Chen et al. [7]. Each 3D segmentation map used for assessing test performance is normalized to have zero mean and unit variance.

CHAOS MR \rightarrow Multi-Atlas Labeling Beyond the Cranial Vault: the second domain adaptation task consists of data frames from two different dataset. As source domain we, consider the the 2019 CHAOS MR dataset [28], previously used in the 2019 CHAOS Grad Challenge. The dataset consists of both MR and CT scans with segmentation maps for the following abdominal organs: liver, right kidney, left kidney and spleen. Similar to [7] we use the T2-SPIR MR images as the source domain. Each scan is centered to zero mean and unit variance, and values more than three standard deviations away from the mean are clipped. In total, we obtain 20 MR scans, 16 of which we use for training and 4 for validation. The target domain is represented by the dataset which was presented in the Multi-Atlas Labeling Beyond the Cranial Vault MICCAI 2015 Challenge [34]. We utilize the 30 CT scans in the training set which are provided segmentation maps, and use 24

¹<https://github.com/serbanstan/uda-medical-image-segmentation-sfs>

for adaptation and 6 for evaluating generalization performance. The value range in the CT scans was first clipped to $[-125, 275]$ HU following literature [75]. The images were re-sampled to an axial view size of 256×256 . Background was then cropped such that the distance between any labeled pixel and the image borders is at least 30 pixels, and scans were again resized to 256×256 . Finally, each 3D scan was normalized independently to zero mean and unit variance, and values more than three standard deviation from the mean were clipped. Data augmentation was performed as follows on both the training MR and training CT instances to improve generalization: (1) random rotations of up to 20 degrees, (2) negating pixel values, (3) adding random Gaussian noise, (4) random cropping.

Both of the above problems involve 3D scans. However our network encoder architecture receives 2D images at its input, where each image consists of three channels. To circumvent this discrepancy, we follow the frame-by-frame processing methodology by Chen et al. [6]. We convert higher dimensional features into 2D images by creating images from groups of three consecutive scan slices, and using them as labels for the segmentation map of the middle slice. Implementation details including network architecture, learning schedule, batch selection, optimization, hardware setup, etc. are included in the Appendix.

6.2. Evaluation Methodology

Following the medical image segmentation literature, we use two main metrics for evaluation: dice coefficient and average symmetric surface distance (ASSD). The Dice coefficient is a popular choice in medical image analysis works which measures semantic segmentation quality [6, 7, 75]. It is used for direct evaluation of segmentation map accuracy. The average symmetric surface distance is a metric which has been used [63, 7, 16] to assess the quality of borders of predicted segmentation maps which are important for diagnosis. A good segmentation will have a large Dice coefficient and low ASSD value, the desirability of a result being application dependant.

We compare our approach to other state-of-the-art techniques that are developed for unsupervised medical image segmentation. To the best of our knowledge, no prior work addresses source-free UDA for semantic segmentation, so we compare our work against existing UDA techniques that need source data for alignment. We compare against adversarial approaches PnP-AdaNet [13], SynSeg-Net [25], AdaOutput [66], CycleGAN [77], CyCADA [23], SIFA [7], ARL-GAN [10], DSFN [79], SASAN [65], DSAN [21]. These works are recently developed methods for semantic segmentation that should serve as upper bounds for our method, because we do not process the source domain data directly. We reiterate that the advantage of our method is to preserve privacy and we do not claim best performance.

6.3. Quantitative and Quantitative Results

Tables 2 and 1 summarize the segmentation performance for our method along with the baselines. We observe our method is comparable to SOTA approaches on the MMWHS dataset, despite the additional source-free constraint, and often outperforms other recently developed methods. We also note that our method outperforms all the listed methods on class AA, while having second best Dice scores on LAC, and competitive performance on the two remaining classes. However, we note that our method trails the other approaches when compared with respect to ASSD. This shows that our domain alignment approach successfully maps each class in the target embedding to its corresponding vicinity using the prototypical distribution, but lacks the refinement offered by adversarial approaches. In our second segmentation task, we observe similar trends. We observe competitive performance against other reported results, especially on classes Liver, L. Kidney and Spleen. These results suggest that our method offers possibility of domain adaptation with competitive performance in a data-private regime. An idea to enhance performance in terms of ASSD is to use parametric distributions that can approximate the prototypical distribution more accurately.

We provide qualitative assessment results. In Figure 5, we present the improvement in segmentation on CT scans from both the cardiac and abdominal organ datasets. In both cases, the supervised models are able to obtain a near perfect visual similarity to the ground truth segmentation mask. These represent the upper bound performance we compare against. Post-adaptation quality of the segmentation maps becomes much closer to the supervised regime from a visual perspective. However, fine details on image borders need more improvement- for example in images 2, 5, 6, 10. This is in line with the observed performance of our model when measured with ASSD. In conclusion, while we observe significant gains with respect to the Dice coefficient which directly measures the segmentation accuracy, the improvement in surface distance is not as large as in methods maintaining access to the source domain during adaptation. However, our performance is competitive given the advantage of providing privacy for the source domain.

6.4. Ablation Studies and Analysis

We empirically demonstrate that our theoretical analysis explains why our algorithm works. To achieve this, we analyze the shift in latent embedding before and after adaptation, and discuss how the ρ parameter influences the prototypical distribution approximation in the latent space. The other hyper-parameter used in our approach, the regularizer λ , was empirically observed to not significantly influence results. In order to visualize these embeddings, we use UMAP [42] which allows for embedding high-dimensional distributions into 2D space for 2D visualization.

Figures 2 and 3 showcases the impact of our algorithm on the latent distribution of the two datasets. In Figure 2a, we record the latent embedding of the GMM prototypical distribution that is learned on the cardiac MR embeddings. Figure 2b exemplifies the distribution of the target CT samples before adaptation. As we can see from Table 1, the source-trained model is able to achieve some level of class separation without any adaptation, which is confirmed in Figure 2b. Even so, we observe non-trivial overlap between the latent embeddings of two of the classes. In Figure 2c we observe that this overlap is reduced after adaptation. We also observe that the latent embedding of the target CT samples is shifted towards the prototypical distribution. For completeness, we repeat the same analysis for the organ segmentation dataset. We observe a similar behavior in the shift of the target embeddings based on the learned prototypical distribution, however compared to the heart segmentation dataset this shift is visually less pronounced.

We also investigate the impact of the value of the ρ parameter on our prototypical distribution. In Figure 4 we present the UMAP visualization for the learned GMM embeddings for three different values of ρ . We observe that while some classes will be separated for $\rho = 0$, selecting high-confident samples to learn the GMM will yield a prototypical distribution with a higher separability. Following Equation 5, we use a value of $\rho = .97$ in our experiments, however we note our algorithm is robust with respect to the value of this parameter if the value is set to be close to 1.

The quality of pixel label shift is analyzed in Tables 3 and 4. In Table 3 we observe that for the cardiac dataset there exists significant inter-class label transfer, for approximately 20% of pixels, evenly distributed across classes. We see the majority of these shifts leading to an improvement in labeling accuracy, including all shifts where at least 1% of labels migrate, which is in line with our other reported results. These findings also corroborate with our observed embeddings. We can see from Table 3 that during adaptation there is significant label migration between *LVC* and *MYO*, and this can be observed in the increased separation between the two classes in Figures 2b and 2c. For the abdominal organ dataset we observe significantly less label shift between classes, with most of the activity involving previously labeled pixels being correctly le-labeled as *Ignore* after adaptation, or pixels initially in *Ignore* being correctly le-labeled to their appropriate class. This again supports the post adaptation improvement gains previously observed.

7. Conclusions

We developed a novel algorithm for performing unsupervised domain adaptation of semantic segmentation models in a source-free learning setting to preserve privacy of data for the source domain. After supervised training on a source

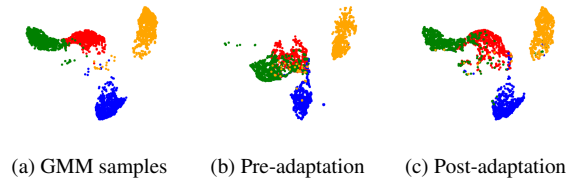


Figure 2: Indirect distribution matching in the embedding space: (a) drawn samples from the GMM trained on the cardiac MR distribution, (b) representations of the cardiac CT test samples prior to model adaptation (c) representation of the cardiac CT test samples after domain alignment. The four colors correspond to the four cardiac classes: *AA*, *LAC*, *LVC*, *MYO*.

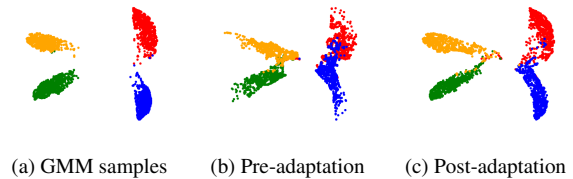


Figure 3: Indirect distribution matching in the embedding space: (a) drawn samples from the GMM trained on the CHAOS MR distribution, (b) representations of the Multi-Atlas CT test samples prior to model adaptation (c) representation of the Multi-Atlas CT test samples after domain alignment. The four colors correspond to the four abdominal organ classes: *liver*, *right kidney*, *left kidney*, *spleen*.

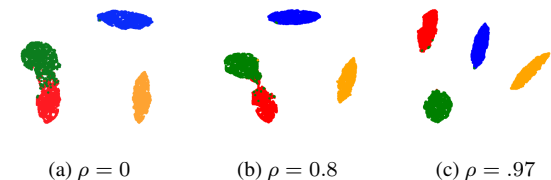


Figure 4: Learnt Gaussian embeddings on the cardiac dataset. From left to right we present samples from the learnt GMM when $\rho = 0$, $\rho = .8$ and $\rho = .97$ respectively.

domain, our algorithm is able to generalize to new domains without having access to source samples. Our idea is based on estimating a prototypical distribution via a GMM and then use is to align two distributions indirectly. We provided theoretical analysis to demonstrated why our method is effective. We also empirically demonstrated that our algorithm is competitive on two real-world datasets when compared against state of the art approaches in medical semantic segmentation that require access to the source data. Moreover, given the source free nature of our adaptation approach, our algorithm is the first of its kind for settings where privacy for source domain is a major concern.

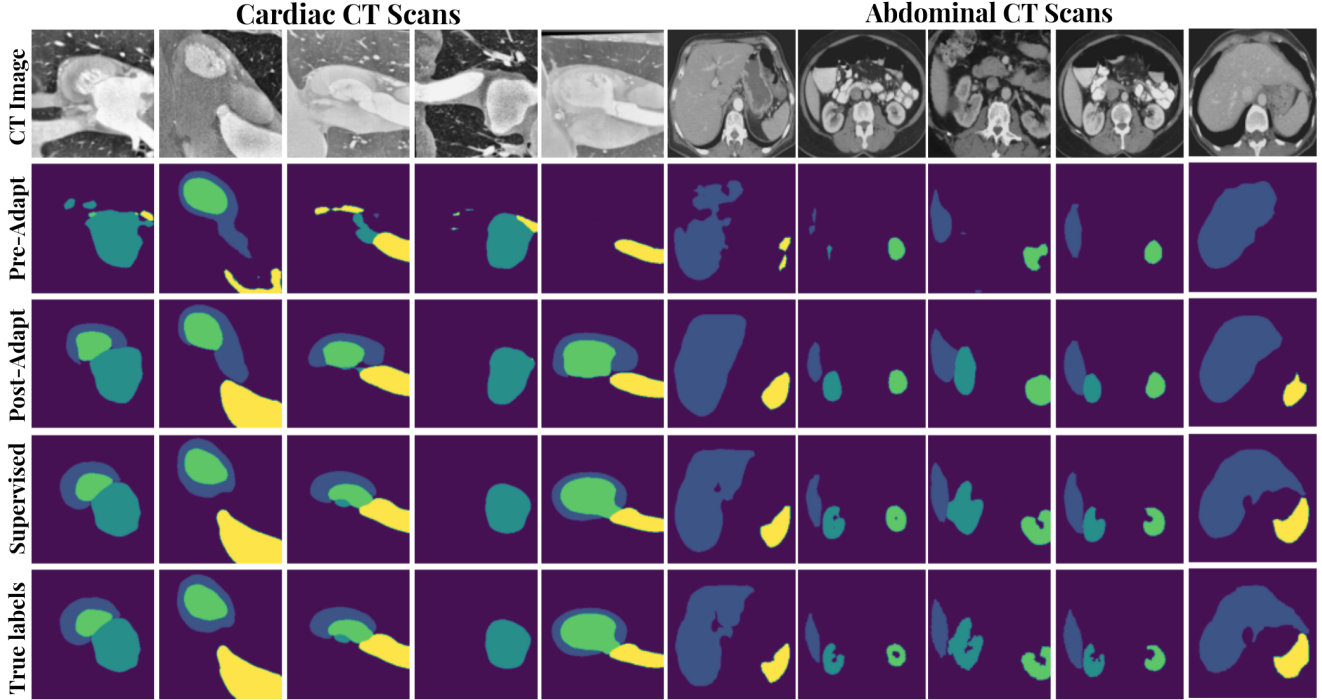


Figure 5: Segmentation maps of CT samples from the two datasets used for evaluation. The first five columns correspond to cardiac images, while the last five columns correspond to abdominal images. From top to bottom: gray-scale CT images, source-only model predictions, post-adaptation model predictions, supervised predictions on the CT data, ground truth.

Method	Dice					Average Symmetric Surface Distance				
	AA	LAC	LVC	MYO	Average	AA	LAC	LVC	MYO	Average
Source-Only	28.4	27.7	4.0	8.7	17.2	20.6	16.2	N/A	48.4	N/A
PnP-AdaNet [13]	74.0	68.9	61.9	50.8	63.9	12.8	6.3	17.4	14.7	12.8
SynSeg-Net [25]	71.6	69.0	51.6	40.8	58.2	11.7	7.8	7.0	9.2	8.9
AdaOutput [66]	65.2	76.6	54.4	43.3	59.9	17.9	5.5	5.9	8.9	9.6
CycleGAN [77]	73.8	75.7	52.3	28.7	57.6	11.5	13.6	9.2	8.8	10.8
CyCADA [23]	72.9	77.0	62.4	45.3	64.4	9.6	8.0	9.6	10.5	9.4
SIFA [7]	81.3	79.5	73.8	61.6	74.1	7.9	6.2	5.5	8.5	7.0
ARL-GAN [10]	71.3	80.6	69.5	81.6	75.7	6.3	5.9	6.7	6.5	6.4
DSFN [79]	84.7	76.9	79.1	62.4	75.8	N/A	N/A	N/A	N/A	N/A
SASAN [65]	82.0	76.0	82.0	72.0	78.0	4.1	8.3	3.5	3.3	4.9
DSAN [21]	79.9	84.7	82.7	66.5	78.5	7.7	6.7	3.8	5.6	5.9
Supervised	88.7	89.3	89.0	88.7	87.2	2.6	4.9	2.2	1.6	3.6
Ours	84.9	83.9	71.2	66.7	76.7	13.3	10	20.7	9.4	13.3

Table 1: Segmentation performance comparison for the Cardiac MR \rightarrow CT adaptation task.

Method	Dice				Average Symmetric Surface Distance					
	Liver	R.Kidney	L.Kidney	Spleen	Average	Liver	R.Kidney	L.Kidney	Spleen	Average
Source-Only	73.1	47.3	57.3	55.1	58.2	2.9	5.6	7.7	7.4	5.9
SynSeg-Net [25]	85.0	82.1	72.7	81.0	80.2	2.2	1.3	2.1	2.0	1.9
AdaOutput [66]	85.4	79.7	79.7	81.7	81.6	1.7	1.2	1.8	1.6	1.6
CycleGAN [77]	83.4	79.3	79.4	77.3	79.9	1.8	1.3	1.2	1.9	1.6
CyCADA [23]	84.5	78.6	80.3	76.9	80.1	2.6	1.4	1.3	1.9	1.8
SIFA [7]	88.0	83.3	80.9	82.6	83.7	1.2	1.0	1.5	1.6	1.3
Supervised	94.2	87.2	88.9	89.1	89.8	1.2	1.2	1.1	1.7	1.3
Ours	87.9	72.1	77.7	80.4	79.5	3.3	6.4	4.2	3.9	4.5

Table 2: Segmentation performance comparison for the Abdominal MR \rightarrow CT adaptation task.

	Ignore	MYO	LAC	LVC	AA
Ignore	97.3 99.3 99.3	1.5 20.3 70.0	0.2 80.2 14.8	0.9 6.2 76.1	0.2 43.8 51.7
MYO	13.2 10.4 89.5	81.6 72.2 72.2	0.1 52.7 0.4	5.2 44.6 54.1	0.0 0.0 0.0
LAC	15.1 45.4 46.3	2.5 2.6 79.7	76.1 88.4 88.4	5.9 7.4 87.4	0.4 5.8 77.0
LVC	0.6 67.7 2.3	16.5 33.4 66.3	0.2 83.8 13.0	82.7 92.4 92.4	0.0 93.3 0.0
AA	18.5 7.8 90.9	0.0 0.0 43.7	1.3 5.7 6.2	0.1 0.0 12.9	80.1 91.2 91.2

Table 3: The percentage of shift in pixel labels during adaptation for the cardiac dataset. A cell (i, j) in the table has three values. The first value represents the percentage of pixels labeled i that are labeled j after adaptation. The second value represents the percentage of switching pixels whose true label is i - lower is better. The third value represents the percentage of switching pixels whose true label is j - higher is better. Bolded cells denote label shift where more than 1% of pixels migrate from i to j .

	Ignore	Liver	R. Kidney	L. Kidney	Spleen
Ignore	94.6 98.4 98.4	3.0 18.0 81.6	0.7 23.5 74.3	0.7 34.9 62.6	1.0 19.3 80.5
Liver	6.6 38.1 60.8	92.6 91.3 91.3	0.8 10.4 55.1	0.0 0.0 0.0	0.0 39.0 10.2
R.Kidney	5.0 13.1 86.9	0.2 0.0 76.9	94.8 94.7 94.7	0.0 0.0 0.0	0.0 0.0 0.0
L.Kidney	2.2 24.2 75.0	0.1 0.0 0.0	0.0 23.7 0.0	97.5 87.8 87.8	0.2 0.0 7.2
Spleen	23.1 20.8 79.2	0.1 20.2 0.0	0.2 75.0 0.0	0.0 69.4 0.0	76.6 78.7 78.7

Table 4: The percentage of shift in pixel labels during adaptation for the abdominal organ dataset. The same methodology as in Table 3 is used.

References

- [1] Nicholas Ayache. Deep learning for medical image analysis. In S. Kevin Zhou, Hayit Greenspan, and Dinggang Shen, editors, *Deep Learning for Medical Image Analysis*, page xxiii. Academic Press, 2017. **1**
- [2] Luca Bertinetto, Jack Valmadre, João F. Henriques, Andrea Vedaldi, and Philip H. S. Torr. Fully-convolutional siamese networks for object tracking. In Gang Hua and Hervé Jégou, editors, *Computer Vision – ECCV 2016 Workshops*, pages 850–865, Cham, 2016. Springer International Publishing. **1**
- [3] François Bolley, Arnaud Guillin, and Cédric Villani. Quantitative concentration inequalities for empirical measures on non-compact spaces. *Probability Theory and Related Fields*, 137(3-4):541–593, 2007. **13**
- [4] Konstantinos Bousmalis, Nathan Silberman, David Dohan, Dumitru Erhan, and Dilip Krishnan. Unsupervised pixel-level domain adaptation with generative adversarial networks. In *Proceedings of the IEEE conference on computer vision and pattern recognition*, pages 3722–3731, 2017. **1**
- [5] Cheng Chen, Qi Dou, Hao Chen, and Pheng-Ann Heng. Semantic-aware generative adversarial nets for unsupervised domain adaptation in chest x-ray segmentation. In *International workshop on machine learning in medical imaging*, pages 143–151. Springer, 2018. **2**
- [6] Cheng Chen, Qi Dou, Hao Chen, Jing Qin, and Pheng-Ann Heng. Synergistic image and feature adaptation: Towards cross-modality domain adaptation for medical image segmentation. In *Proceedings of The Thirty-Third Conference on Artificial Intelligence (AAAI)*, pages 865–872, 2019. **6**
- [7] C. Chen, Q. Dou, H. Chen, J. Qin, and P. A. Heng. Unsupervised bidirectional cross-modality adaptation via deeply synergistic image and feature alignment for medical image segmentation. *IEEE Transactions on Medical Imaging*, 39(7):2494–2505, 2020. **5, 6, 8**
- [8] Chaoqi Chen, Weiping Xie, Wenbing Huang, Yu Rong, Xinghao Ding, Yue Huang, Tingyang Xu, and Junzhou Huang. Progressive feature alignment for unsupervised domain adaptation. In *Proceedings of the IEEE Conference on Computer Vision and Pattern Recognition*, pages 627–636, 2019. **1**
- [9] Liang-Chieh Chen, George Papandreou, Iasonas Kokkinos, Kevin Murphy, and Alan L Yuille. Deeplab: Semantic image segmentation with deep convolutional nets, atrous convolution, and fully connected crfs. *IEEE transactions on pattern analysis and machine intelligence*, 40(4):834–848, 2017. **13**
- [10] Xu Chen, Chunfeng Lian, Li Wang, Hannah Deng, Tianshu Kuang, Steve Fung, Jaime Gateno, Pew-Thian Yap, James J Xia, and Dinggang Shen. Anatomy-regularized representation learning for cross-modality medical image segmentation. *IEEE Transactions on Medical Imaging*, 40(1):274–285, 2020. **6, 8**
- [11] Jaehoon Choi, Taekyung Kim, and Changick Kim. Self-ensembling with gan-based data augmentation for domain adaptation in semantic segmentation. In *Proceedings of the IEEE international conference on computer vision*, pages 6830–6840, 2019. **1**
- [12] Nicolas Courty, Rémi Flamary, Devis Tuia, and Alain Rakotomamonjy. Optimal transport for domain adaptation. *IEEE transactions on pattern analysis and machine intelligence*, 39(9):1853–1865, 2016. **2**
- [13] Qi Dou, Cheng Ouyang, Cheng Chen, Hao Chen, Ben Glocker, Xiahai Zhuang, and Pheng-Ann Heng. Pnp-adanet: Plug-and-play adversarial domain adaptation network at unpaired cross-modality cardiac segmentation. *IEEE Access*, 7:99065–99076, 2019. **1, 6, 8**
- [14] Qi Dou, Cheng Ouyang, Cheng Chen, Hao Chen, and Pheng-Ann Heng. Unsupervised cross-modality domain adaptation of convnets for biomedical image segmentations with adversarial loss. *arXiv:1804.10916 [cs]*, Jun 2018. arXiv: 1804.10916. **2**
- [15] Qi Dou, Cheng Ouyang, Cheng Chen, Hao Chen, and Pheng-Ann Heng. Unsupervised cross-modality domain adaptation of convnets for biomedical image segmentations with adversarial loss. In *Proceedings of the 27th International Joint Conference on Artificial Intelligence (IJCAI)*, pages 691–697, 2018. **5**
- [16] Qi Dou, Lequan Yu, Hao Chen, Yueming Jin, Xin Yang, Jing Qin, and Pheng-Ann Heng. 3d deeply supervised network for automated segmentation of volumetric medical images. *Medical Image Analysis*, 41:40 – 54, 2017. Special Issue on the 2016 Conference on Medical Image Computing and Computer Assisted Intervention (Analog to MICCAI 2015). **6**
- [17] K. Drossos, P. Magron, and T. Virtanen. Unsupervised adversarial domain adaptation based on the wasserstein distance for acoustic scene classification. In *2019 IEEE Workshop on Applications of Signal Processing to Audio and Acoustics (WASPAA)*, pages 259–263, 2019. **2**
- [18] Charlie Frogner, Chiyuan Zhang, Hossein Mobahi, Mauricio Araya, and Tomaso A Poggio. Learning with a wasserstein loss. In *Advances in neural information processing systems*, pages 2053–2061, 2015. **4**
- [19] Alberto Garcia-Garcia, Sergio Orts-Escolano, Sergiu Oprea, Victor Villena-Martinez, and Jose Garcia-Rodriguez. A review on deep learning techniques applied to semantic segmentation. *arXiv preprint arXiv:1704.06857*, 2017. **2**
- [20] Muhammad Ghifary, W Bastiaan Kleijn, Mengjie Zhang, David Balduzzi, and Wen Li. Deep reconstruction-classification networks for unsupervised domain adaptation. In *European Conference on Computer Vision*, pages 597–613. Springer, 2016. **1**
- [21] Xiaoting Han, Lei Qi, Qian Yu, Ziqi Zhou, Yefeng Zheng, Yinghuan Shi, and Yang Gao. Deep symmetric adaptation network for cross-modality medical image segmentation. *arXiv preprint arXiv:2101.06853*, 2021. **6, 8**
- [22] Simon Hecker, Dengxin Dai, and Luc Van Gool. End-to-end learning of driving models with surround-view cameras and route planners. In *Proceedings of the European Conference on Computer Vision (ECCV)*, September 2018. **1**
- [23] Judy Hoffman, Eric Tzeng, Taesung Park, Jun-Yan Zhu, Phillip Isola, Kate Saenko, Alexei Efros, and Trevor Darrell. Cycada: Cycle-consistent adversarial domain adaptation. In *International conference on machine learning*, pages 1989–1998. PMLR, 2018. **1, 2, 6, 8**

- [24] Yuankai Huo, Zhoubing Xu, Shunxing Bao, Albert Assad, Richard G Abramson, and Bennett A Landman. Adversarial synthesis learning enables segmentation without target modality ground truth. In *2018 IEEE 15th international symposium on biomedical imaging (ISBI 2018)*, pages 1217–1220. IEEE, 2018. [2](#)
- [25] Yuankai Huo, Zhoubing Xu, Hyeonsoo Moon, Shunxing Bao, Albert Assad, Tamara K. Moyo, Michael R. Savona, Richard G. Abramson, and Bennett A. Landman. Synseg-net: Synthetic segmentation without target modality ground truth. *IEEE Transactions on Medical Imaging*, 38(4):1016–1025, Apr 2019. [6](#), [8](#)
- [26] Konstantinos Kamnitsas, Christian Baumgartner, Christian Ledig, Virginia Newcombe, Joanna Simpson, Andrew Kane, David Menon, Aditya Nori, Antonio Criminisi, Daniel Rueckert, et al. Unsupervised domain adaptation in brain lesion segmentation with adversarial networks. In *International conference on information processing in medical imaging*, pages 597–609. Springer, 2017. [2](#)
- [27] Konstantinos Kamnitsas, Christian Baumgartner, Christian Ledig, Virginia Newcombe, Joanna Simpson, Andrew Kane, David Menon, Aditya Nori, Antonio Criminisi, Daniel Rueckert, and Ben Glocker. Unsupervised domain adaptation in brain lesion segmentation with adversarial networks. In Marc Niethammer, Martin Styner, Stephen Aylward, Hongtu Zhu, Ipek Oguz, Pew-Thian Yap, and Dinggang Shen, editors, *Information Processing in Medical Imaging*, pages 597–609, Cham, 2017. Springer International Publishing. [2](#)
- [28] Ali Emre Kavur, M Alper Selver, Oguz Dicle, Mustafa Baris, and N Sinem Gezer. Chaos-combined (ct-mr) healthy abdominal organ segmentation challenge data, Apr 2019. [5](#)
- [29] Salome Kazemina, Christoph Baur, Arjan Kuijper, Bram van Ginneken, Nassir Navab, Shadi Albarqouni, and Anirban Mukhopadhyay. Gans for medical image analysis. *Artificial Intelligence in Medicine*, 109:101938, 2020. [1](#)
- [30] J. Ker, L. Wang, J. Rao, and T. Lim. Deep learning applications in medical image analysis. *IEEE Access*, 6:9375–9389, 2018. [1](#)
- [31] Jinkyu Kim and John Canny. Interpretable learning for self-driving cars by visualizing causal attention. In *Proceedings of the IEEE International Conference on Computer Vision (ICCV)*, Oct 2017. [1](#)
- [32] Soheil Kolouri, Kimia Nadjahi, Umut Simsekli, Roland Badeau, and Gustavo Rohde. Generalized sliced wasserstein distances. In *Advances in Neural Information Processing Systems*, pages 261–272, 2019. [4](#)
- [33] Jogendra Nath Kundu, Naveen Venkat, R Venkatesh Babu, et al. Universal source-free domain adaptation. In *Proceedings of the IEEE/CVF Conference on Computer Vision and Pattern Recognition*, pages 4544–4553, 2020. [1](#), [2](#)
- [34] Bennett Landman, Z Xu, JE Igelsias, M Styner, TR Langerak, and A Klein. Multi-atlas labeling beyond the cranial vault-workshop and challenge, 2015. [5](#)
- [35] Tien-Nam Le, Amaury Habrard, and Marc Sebban. Deep multi-wasserstein unsupervised domain adaptation. *Pattern Recognition Letters*, 125:249 – 255, 2019. [2](#)
- [36] Chen-Yu Lee, Tanmay Batra, Mohammad Haris Baig, and Daniel Ulbricht. Sliced wasserstein discrepancy for unsupervised domain adaptation. In *Proceedings of the IEEE Conference on Computer Vision and Pattern Recognition*, pages 10285–10295, 2019. [1](#), [2](#)
- [37] Guosheng Lin, Anton Milan, Chunhua Shen, and Ian Reid. Refinenet: Multi-path refinement networks for high-resolution semantic segmentation. In *Proceedings of the IEEE conference on computer vision and pattern recognition*, pages 1925–1934, 2017. [2](#)
- [38] Dingding Liu, Yingen Xiong, Kari Pulli, and Linda Shapiro. Estimating image segmentation difficulty. In *Machine Learning and Data Mining in Pattern Recognition*, volume 6871, pages 484–495, 08 2011. [1](#)
- [39] D. Liu, D. Zhang, Y. Song, F. Zhang, L. O’Donnell, H. Huang, M. Chen, and W. Cai. Pdam: A panoptic-level feature alignment framework for unsupervised domain adaptive instance segmentation in microscopy images. *IEEE Transactions on Medical Imaging*, pages 1–1, 2020. [2](#)
- [40] Jonathan Long, Evan Shelhamer, and Trevor Darrell. Fully convolutional networks for semantic segmentation. In *Proceedings of the IEEE conference on computer vision and pattern recognition*, pages 3431–3440, 2015. [2](#)
- [41] Xinhong Ma, Tianzhu Zhang, and Changsheng Xu. Gcan: Graph convolutional adversarial network for unsupervised domain adaptation. In *Proceedings of the IEEE/CVF Conference on Computer Vision and Pattern Recognition (CVPR)*, June 2019. [2](#)
- [42] Leland McInnes, John Healy, and James Melville. Umap: Uniform manifold approximation and projection for dimension reduction, 2020. [6](#)
- [43] Quentin Mérigot. A multiscale approach to optimal transport. In *Computer Graphics Forum*, volume 30, pages 1583–1592. Wiley Online Library, 2011. [4](#)
- [44] Saeid Motiian, Quinn Jones, Seyed Iranmanesh, and Gianfranco Doretto. Few-shot adversarial domain adaptation. In *Advances in Neural Information Processing Systems*, pages 6670–6680, 2017. [2](#)
- [45] Hyeonwoo Noh, Seunghoon Hong, and Bohyung Han. Learning deconvolution network for semantic segmentation. In *Proceedings of the IEEE international conference on computer vision*, pages 1520–1528, 2015. [2](#)
- [46] Yingwei Pan, Ting Yao, Yehao Li, Yu Wang, Chong-Wah Ngo, and Tao Mei. Transferrable prototypical networks for unsupervised domain adaptation. In *Proceedings of the IEEE Conference on Computer Vision and Pattern Recognition*, pages 2239–2247, 2019. [2](#)
- [47] Ievgen Redko, Amaury Habrard, and Marc Sebban. Theoretical analysis of domain adaptation with optimal transport. In *Joint European Conference on Machine Learning and Knowledge Discovery in Databases*, pages 737–753. Springer, 2017. [13](#)
- [48] Mohammad Rostami. *Learning Transferable Knowledge Through Embedding Spaces*. PhD thesis, University of Pennsylvania, 2019. [2](#)
- [49] Mohammad Rostami and Aram Galstyan. Sequential unsupervised domain adaptation through prototypical distributions. *arXiv preprint arXiv:2007.00197*, 2020. [1](#)

- [50] Mohammad Rostami and Aram Galstyan. Domain adaptation for sentiment analysis using increased intraclass separation. *arXiv preprint arXiv:2107.01598*, 2021. **2**
- [51] Mohammad Rostami, David Huber, and Tsai-Ching Lu. A crowdsourcing triage algorithm for geopolitical event forecasting. In *Proceedings of the 12th ACM Conference on Recommender Systems*, pages 377–381, 2018. **1**
- [52] Mohammad Rostami, Soheil Kolouri, Eric Eaton, and Kyungnam Kim. Deep transfer learning for few-shot sar image classification. *Remote Sensing*, 11(11):1374, 2019. **2**
- [53] Mohammad Rostami, Soheil Kolouri, Eric Eaton, and Kyungnam Kim. Sar image classification using few-shot cross-domain transfer learning. In *Proceedings of the IEEE/CVF Conference on Computer Vision and Pattern Recognition Workshops*, pages 0–0, 2019. **2**
- [54] Mohammad Rostami, Soheil Kolouri, and Praveen K Pilly. Complementary learning for overcoming catastrophic forgetting using experience replay. In *Proceedings of the 28th International Joint Conference on Artificial Intelligence*, pages 3339–3345. AAAI Press, 2019. **2**
- [55] Mohammad Rostami, Soheil Kolouri, Praveen K Pilly, and James McClelland. Generative continual concept learning. In *AAAI*, pages 5545–5552, 2020. **2**
- [56] Kuniaki Saito, Kohei Watanabe, Yoshitaka Ushiku, and Tatsuya Harada. Maximum classifier discrepancy for unsupervised domain adaptation. In *Proceedings of the IEEE Conference on Computer Vision and Pattern Recognition*, pages 3723–3732, 2018. **1, 2**
- [57] Cristiano Saltori, Stéphane Lathuilière, Nicu Sebe, Elisa Ricci, and Fabio Galasso. Sf-uda3d: Source-free unsupervised domain adaptation for lidar-based 3d object detection. *arXiv preprint arXiv:2010.08243*, 2020. **1, 2**
- [58] Swami Sankaranarayanan, Yogesh Balaji, Carlos D Castillo, and Rama Chellappa. Generate to adapt: Aligning domains using generative adversarial networks. In *Proceedings of the IEEE Conference on Computer Vision and Pattern Recognition*, pages 8503–8512, 2018. **1**
- [59] Dinggang Shen, Guorong Wu, and Heung-Il Suk. Deep learning in medical image analysis. *Annual Review of Biomedical Engineering*, 19(1):221–248, 2017. PMID: 28301734. **1**
- [60] Karen Simonyan and Andrew Zisserman. Very deep convolutional networks for large-scale image recognition, 2015. **13**
- [61] Serban Stan and Mohammad Rostami. Unsupervised model adaptation for continual semantic segmentation. In *Proceedings of the AAAI Conference on Artificial Intelligence*, volume 35, pages 2593–2601, 2021. **2**
- [62] Baochen Sun, Jiashi Feng, and Kate Saenko. Correlation alignment for unsupervised domain adaptation. In *Domain Adaptation in Computer Vision Applications*, pages 153–171. Springer, 2017. **1**
- [63] Changjian Sun, Shuxu Guo, Huimao Zhang, Jing Li, Meimei Chen, Shuzhi Ma, Lanyi Jin, Xiaoming Liu, Xueyan Li, and Xiaohua Qian. Automatic segmentation of liver tumors from multiphase contrast-enhanced ct images based on fcns. *Artificial Intelligence in Medicine*, 83:58 – 66, 2017. Machine Learning and Graph Analytics in Computational Biomedicine. **6**
- [64] Marco Toldo, Andrea Maracani, Umberto Michieli, and Pietro Zanuttigh. Unsupervised domain adaptation in semantic segmentation: A review. *Technologies*, 8(2):35, Jun 2020. **1**
- [65] Devavrat Tomar, Manana Lortkipanidze, Guillaume Vray, Behzad Bozorgtabar, and Jean-Philippe Thiran. Self-attentive spatial adaptive normalization for cross-modality domain adaptation. *IEEE Transactions on Medical Imaging*, 2021. **6, 8**
- [66] Y.-H. Tsai, W.-C. Hung, S. Schuster, K. Sohn, M.-H. Yang, and M. Chandraker. Learning to adapt structured output space for semantic segmentation. In *IEEE Conference on Computer Vision and Pattern Recognition (CVPR)*, 2018. **6, 8**
- [67] Eric Tzeng, Judy Hoffman, Kate Saenko, and Trevor Darrell. Adversarial discriminative domain adaptation. In *Proceedings of the IEEE conference on computer vision and pattern recognition*, pages 7167–7176, 2017. **1**
- [68] Hemanth Venkateswara, Jose Eusebio, Shayok Chakraborty, and Sethuraman Panchanathan. Deep hashing network for unsupervised domain adaptation. In *Proceedings of the IEEE Conference on Computer Vision and Pattern Recognition*, pages 5018–5027, 2017. **1**
- [69] Alper Yilmaz, Omar Javed, and Mubarak Shah. Object tracking: A survey. *ACM Comput. Surv.*, 38(4):13–es, Dec. 2006. **1**
- [70] Junyi Zhang, Ziliang Chen, Junying Huang, Liang Lin, and Dongyu Zhang. Few-shot structured domain adaptation for virtual-to-real scene parsing. In *Proceedings of the IEEE International Conference on Computer Vision Workshops*, pages 0–0, 2019. **2**
- [71] Weichen Zhang, Wanli Ouyang, Wen Li, and Dong Xu. Collaborative and adversarial network for unsupervised domain adaptation. In *Proceedings of the IEEE Conference on Computer Vision and Pattern Recognition*, pages 3801–3809, 2018. **1**
- [72] Weichen Zhang, Wanli Ouyang, Wen Li, and Dong Xu. Collaborative and adversarial network for unsupervised domain adaptation. In *Proceedings of the IEEE Conference on Computer Vision and Pattern Recognition (CVPR)*, June 2018. **2**
- [73] Yue Zhang, Shun Miao, Tommaso Mansi, and Rui Liao. Task driven generative modeling for unsupervised domain adaptation: Application to x-ray image segmentation. In *International Conference on Medical Image Computing and Computer-Assisted Intervention*, pages 599–607. Springer, 2018. **2**
- [74] Yu Zhao, Hongwei Li, Shaohua Wan, Anjany Sekuboyina, Xiaobin Hu, Giles Tetteh, Marie Piraud, and Bjoern Menze. Knowledge-aided convolutional neural network for small organ segmentation. *IEEE journal of biomedical and health informatics*, 23(4):1363–1373, 2019. **1**
- [75] Yuyin Zhou, Zhe Li, Song Bai, Chong Wang, Xinlei Chen, Mei Han, Elliot Fishman, and Alan Yuille. Prior-aware neural network for partially-supervised multi-organ segmentation, 2019. **6**

- [76] Ji Zhu, Hua Yang, Nian Liu, Minyoung Kim, Wenjun Zhang, and Ming-Hsuan Yang. Online multi-object tracking with dual matching attention networks. In *Proceedings of the European Conference on Computer Vision (ECCV)*, September 2018. 1
- [77] Jun-Yan Zhu, Taesung Park, Phillip Isola, and Alexei A. Efros. Unpaired image-to-image translation using cycle-consistent adversarial networks, 2020. 6, 8
- [78] Xiahai Zhuang and Juan Shen. Multi-scale patch and multi-modality atlases for whole heart segmentation of mri. *Medical Image Analysis*, 31:77 – 87, 2016. 5
- [79] Danbing Zou, Qikui Zhu, and Pingkun Yan. Unsupervised domain adaptation with dual scheme fusion network for medical image segmentation. In *Proceedings of the Twenty-Ninth International Joint Conference on Artificial Intelligence, IJCAI-20, International Joint Conferences on Artificial Intelligence Organization*, pages 3291–3298, 2020. 6, 8

8. Appendix

8.1. Theoretical Analysis

We use a result by Redko et al. [47] which is developed for domain adaptation based on joint training.

Theorem 2 (Redko et al. [47]): Consider that a model is trained on the source domain, then for any $d' > d$ and $\zeta < \sqrt{2}$, there exists a constant number N_0 depending on d' such that for any $\xi > 0$ and $\min(N, M) \geq \max(\xi^{-(d'+2)}, 1)$ with probability at least $1 - \xi$, the following holds:

$$e_{\mathcal{T}} \leq e_{\mathcal{S}} + W(\hat{\mu}_{\mathcal{T}}, \hat{\mu}_{\mathcal{S}}) + e_{\mathcal{C}}(\mathbf{w}^*) + \sqrt{(2 \log(\frac{1}{\xi})/\zeta)} \left(\sqrt{\frac{1}{N}} + \sqrt{\frac{1}{M}} \right). \quad (6)$$

Theorem 2 relates the performance of a source-trained model on a target domain through an upperbound which depends on the distance between the source and the target domain distributions in terms WD distance. We use Theorem 2 to deduce Theorem 1 in the paper. Redko et al. [47] provide their analysis for the case of binary classifier but their analysis can be extended to multiclass scenario.

Theorem 1 : Consider that we generate a pseudo-dataset using the prototypical distribution and preform UDA according to algorithm 1, then:

$$e_{\mathcal{T}} \leq e_{\mathcal{S}} + W(\hat{\mu}_{\mathcal{S}}, \hat{\mu}_{\mathcal{P}}) + W(\hat{\mu}_{\mathcal{T}}, \hat{\mu}_{\mathcal{P}}) + (1 - \rho) + e_{\mathcal{C}'}(\mathbf{w}^*) + \sqrt{(2 \log(\frac{1}{\xi})/\zeta)} \left(\sqrt{\frac{1}{N}} + \sqrt{\frac{1}{M}} + 2\sqrt{\frac{1}{N_p}} \right), \quad (7)$$

where $W(\cdot, \cdot)$ denotes the WD distance and ξ is a constant, dependent on the loss function $\mathcal{L}(\cdot)$.

Proof: Since we use the parameter ρ to estimate the prototypical distribution, the probability of predicting incorrect labels for the drawn pseudo-data points is $1 - \rho$. We can define the following difference:

$$|\mathcal{L}(\phi_{w_0}(\mathbf{z}_i^p), \mathbf{y}_i^p) - \mathcal{L}(\phi_{w_0}(\mathbf{z}_i^p), \hat{\mathbf{y}}_i^p)| = \begin{cases} 0, & \text{if } \mathbf{y}_i^p = \hat{\mathbf{y}}_i^p. \\ 1, & \text{otherwise.} \end{cases} \quad (8)$$

We can apply Jensen's inequality following taking the expectation with respect to the target domain distribution in the embedding space, i.e., $\chi \circ \psi(p^t(\mathbf{X}^T))$, on both sides of Eq. (8) and conclude:

$$|e_{\mathcal{P}} - e_{\mathcal{T}}| \leq \mathbb{E}(|\mathcal{L}(\phi_{w_0}(\mathbf{z}_i^p), \mathbf{y}_i^p) - \mathcal{L}(\phi_{w_0}(\mathbf{z}_i^p), \hat{\mathbf{y}}_i^p)|) \leq (1 - \rho). \quad (9)$$

Now we use Eq. (9) to deduce:

$$e_{\mathcal{S}} + e_{\mathcal{T}} = e_{\mathcal{S}} + e_{\mathcal{T}} + e_{\mathcal{P}} - e_{\mathcal{P}} \leq e_{\mathcal{S}} + e_{\mathcal{P}} + |e_{\mathcal{T}} - e_{\mathcal{P}}| \leq e_{\mathcal{S}} + e_{\mathcal{P}} + (1 - \rho). \quad (10)$$

Taking infimum on both sides of Eq. (10) and employing the definition of the joint optimal model yields:

$$e_{\mathcal{C}}(\mathbf{w}^*) \leq e_{\mathcal{C}'}(\mathbf{w}) + (1 - \rho). \quad (11)$$

Now we consider Theorem 2 by Redko et al. [47] for the source and target domains in our problem and merge Eq. (11) on Eq.(6) to conclude:

$$e_{\mathcal{T}} \leq e_{\mathcal{S}} + W(\hat{\mu}_{\mathcal{T}}, \hat{\mu}_{\mathcal{S}}) + e_{\mathcal{C}'}(\mathbf{w}^*) + (1 - \rho) + \sqrt{(2 \log(\frac{1}{\xi})/\zeta)} \left(\sqrt{\frac{1}{N}} + \sqrt{\frac{1}{M}} \right). \quad (12)$$

In Eq. (12), $e_{\mathcal{C}'}$ denotes the joint optimal model true error for the source domain and the pseudo-dataset as the second domain.

Now we apply the triangular inequality twice in Eq. (12) to deduce:

$$W(\hat{\mu}_{\mathcal{T}}, \hat{\mu}_{\mathcal{S}}) \leq W(\hat{\mu}_{\mathcal{T}}, \mu_{\mathcal{P}}) + W(\hat{\mu}_{\mathcal{S}}, \mu_{\mathcal{P}}) \leq W(\hat{\mu}_{\mathcal{T}}, \hat{\mu}_{\mathcal{P}}) + W(\hat{\mu}_{\mathcal{S}}, \hat{\mu}_{\mathcal{P}}) + 2W(\hat{\mu}_{\mathcal{P}}, \mu_{\mathcal{P}}). \quad (13)$$

We now need Theorem 1.1 by Bolley et al. [3] to simplify the term $W(\hat{\mu}_{\mathcal{P}}, \mu_{\mathcal{P}})$ in Eq. (13).

Theorem 3 (Theorem 1.1 by Bolley et al. [3]): consider that $p(\cdot) \in \mathcal{P}(\mathcal{Z})$ and $\int_{\mathcal{Z}} \exp(\alpha \|\mathbf{x}\|_2^2) dp(\mathbf{x}) < \infty$ for some $\alpha > 0$. Let $\hat{p}(\mathbf{x}) = \frac{1}{N} \sum_i \delta(\mathbf{x}_i)$ denote the empirical distribution that is built from the samples $\{\mathbf{x}_i\}_{i=1}^N$ that are drawn i.i.d from $\mathbf{x}_i \sim p(\mathbf{x})$. Then for any $d' > d$ and $\xi < \sqrt{2}$, there exists N_0 such that for any $\epsilon > 0$ and $N \geq N_0 \max(1, \epsilon^{-(d'+2)})$, we have:

$$P(W(p, \hat{p}) > \epsilon) \leq \exp(-\frac{\xi}{2} N \epsilon^2) \quad (14)$$

This theorem provides a relation to measure the distance between the estimated empirical distribution and the true distribution when the distance is measured by the WD metric.

We can use both Eq. (13) and Eq. (14) in Eq. (12) to conclude Theorem 2 as stated in the paper:

$$e_{\mathcal{T}} \leq e_{\mathcal{S}} + W(\hat{\mu}_{\mathcal{S}}, \hat{\mu}_{\mathcal{P}}) + W(\hat{\mu}_{\mathcal{T}}, \hat{\mu}_{\mathcal{P}}) + (1 - \rho) + e_{\mathcal{C}'}(\mathbf{w}^*) + \sqrt{(2 \log(\frac{1}{\xi})/\zeta)} \left(\sqrt{\frac{1}{N}} + \sqrt{\frac{1}{M}} + 2\sqrt{\frac{1}{N_p}} \right), \quad (15)$$

8.2. Experimental Setup

We use the same network architecture on both the cardiac and organ image segmentation UDA task. We use a DeepLabV3 feature extractor [9] with a VGG16 backbone [60], followed by a one layer classifier.

We train the network on the supervised source samples with a training schedule of 30, 000 epochs repeated 3 times. The optimizer of choice is Adam with learning rate $1e - 4$,

$\epsilon = 1e - 6$ and decay of $1e - 6$. We use the standard pixel-wise cross entropy loss, and batch size of 16. For the abdominal organ segmentation dataset, we observed better performance by using a weighted cross entropy loss, dropout rate of .5.

We learn the empirical prototypical distribution using a parameter $\rho = .97$. We observed good separability in the latent distribution for $\rho \geq .9$.

Finally, when performing adaptation, we performed 30,000 epochs of training, with a batch size of 20. We again use an Adam optimizer with a learning rate of $5e - 5$, $\epsilon = 1e - 1$ and decay of $1e - 6$. Due to GPU memory constraints leading to label distribution shifts between target batches, we approximate the target distribution via the batch label distribution when sampling from the learnt GMMs.

Experiments were done on a Nvidia Titan Xp GPU. Code is provided in the supplementary material section of this submission, and will be made freely available online at a later date.

8.3. Ablation Studies - Continued

We further empirically analyze different components of our approach to demonstrate their effectiveness.

Fine-tuning the classifier. As we discussed in the main body of the paper, after learning a prototypical distribution characterizing the source embeddings, we align the target embeddings to this distribution by minimizing Sliced Wasserstein Distance. In addition, we also further train the classifier on samples from this distribution to account for differences to the original source embedding distribution. We next discuss the benefit of fine tuning the classifier, based on the results in Table 5.

Metric	Fine-Tuned Classifier	Source Domain Classifier
Dice	76.7	75.0
ASSD	13.3	16.7

Table 5: Target performance on the MMWHS adaptation task of our method with and without fine tuning the classifier on samples from the prototypical distribution.

Given the learnt empirical means and covariances for the prototypical distribution, we compare the performance after target domain adaptation between a model that fine tunes the classifier and a model that does not update the classifier after source training. As expected, we can observe fine tuning the classifier offers a prediction boost, even if the difference is not a significant one. The prototypical distribution is meant to encourage the target embeddings to share a similar latent space with the source embeddings, and fine tuning the classifier accounts for the distribution shift between the source embeddings and learnt prototypical distribution.

Impact of warm start on adaptation performance. When performing adaptation, our architecture is initialized

with weights learnt on the source domain. If weights were randomly initialized, the network would be unable to learn boundary features of organs during the adaptation step, and would just perform distribution matching to the GMM embedding. This is confirmed in practice, as initializing the network with random weights before adaptation grants a Dice value of only 5, and observed ASSD of 81.5.

We also investigate the information encoded in the convolutional filters before and after adaptation. Based on our results, we expect network filters to retain most of their structure from source training, and not alter this structure too much during distribution matching. We exemplify this in Figure 6. We record the visual characteristics of the network filters after the first two convolutional layers and the first four convolutional layers. We observe filters appear visually similar before and after adaptation, signifying image structural features learnt by the network do not undergo significant change, even though changes in filter values can be observed under the *Difference* columns.

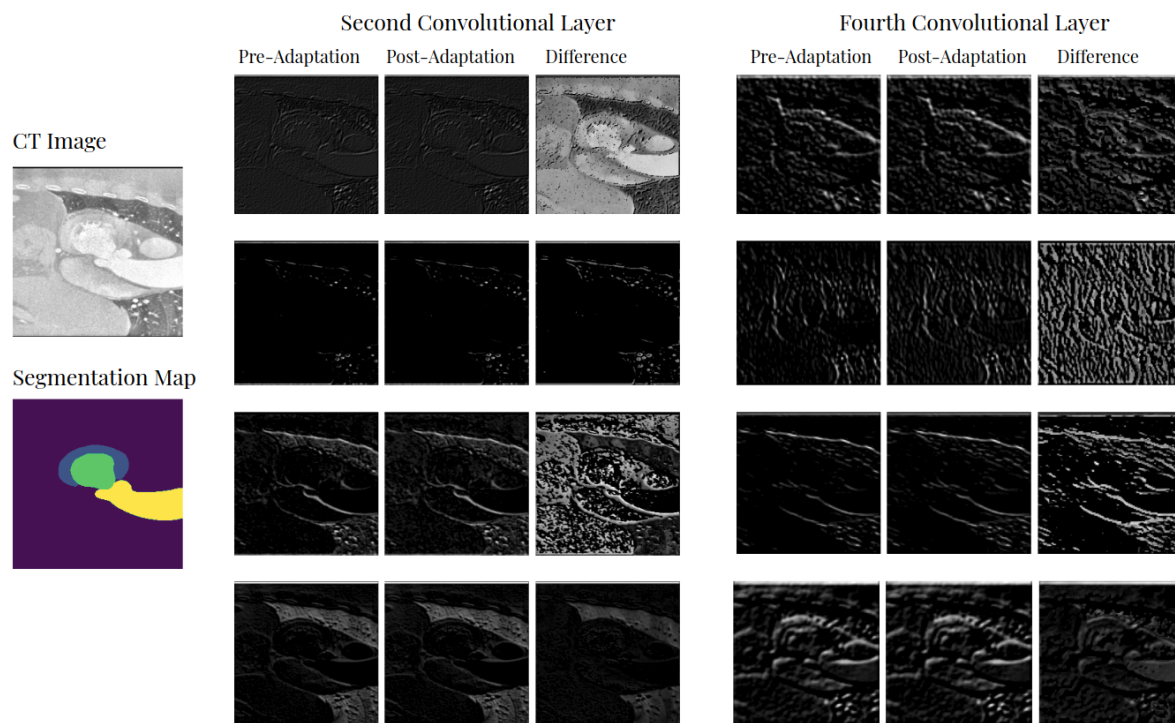


Figure 6: Filter maps of a cardiac CT image before and after model adaptation. In the case of filter differences in absolute value, dark grey symbolizes lower values, while light gray symbolizes higher values.